Harmonic Domain SISO Equivalent Impedance Modeling and Stability Analysis of a Single-phase Grid Connected VSC

Chen Zhang, Marta Molinas, *Member, IEEE,* Sjur Føyen, Jon Are Suul, Takanori Isobe

***Abstract*— This paper presents a harmonic-domain single-input single-output (SISO) equivalent modeling technique for the impedance modeling and stability analysis of a single-phase grid-connected Voltage Source Converter (VSC). The basis is a conversion technique that transforms a harmonic-transfer-function (HTF)-based model into a SISO equivalent model while preserving all the information of frequency couplings. The proposed SISO modeling concept is useful for understanding the meaning and consequence of SISO impedance measurement of an interconnected system with frequency couplings which further enables a simpler impedance measurement and impedance-based analysis. Applications of this method for the VSC model reduction and stability characteristic analyses are presented, from which some useful conclusions regarding the accuracy of three types of reduced-order VSC impedance models and the stability effects of the VSC control with and without compensation for dc voltage variation are obtained. Also, these examples of applications demonstrate how the presented SISO modeling technique facilitates a simpler and efficient impedance-based analysis. Finally, experimental results verify the validity of the proposed VSC-SISO admittance and corresponding analyses.**

***Index Terms*—impedance, Nyquist, SISO, stability, VSC**

I. Introduction

VOLTAGE source converters (VSCs) are being commonly utilized in electrical systems due to their flexibility and controllability. Common applications include grid-integration of wind/photovoltaic power generation [1], interconnection of AC systems through the high-voltage dc (HVDC) transmissions [2], as well as electric drive systems for locomotives [3], etc. With the increasing penetration of VSCs in power systems, interactions among the VSCs and the grid can lead to small-signal instability, e.g. oscillations in [4] and [5]. Thus, it is necessary to analyze the small-signal behavior of VSCs and its consequences on stability. In this respect, the impedance-based method can be applied and is gaining popularity since the impedance of the VSC can be readily derived either from analytical modeling or measurement [6]-[9].

In terms of the impedance modeling, there are two main methods: the linear-time-invariant (LTI) framework-based and the linear-time-periodic (LTP) framework-based methods [7]. The former one usually applies to VSCs whose linearized models can be represented as LTI systems via transformations (e.g. *dq*-transformation). Therefore, corresponding impedance models can be readily obtained by using the Laplace transform or the complex-vector notation [8]. Impedance modeling of a three-phase VSC under this method is for instance discussed in [9]-[11]. On the other hand, if such an equivalent LTI model is unachievable, then the impedance modeling has to be conducted directly on the original linearized system which is an LTP system in general. In this regard, the harmonic linearization method based on the principle of harmonic balance [12] can be adopted. Applications of this method in deriving the impedances of a single-phase VSC, a three-phase VSC and a modular-multi-level-converter (MMC) [13] are presented in [14], [15] and [16] respectively.

Recent analyses have shown VSCs generally exhibit frequency coupling behavior and the number of coupled frequencies depends on the studied topology. For example, the number of frequency couplings in a three-phase VSC is typically bounded by two [17]-[19], which is interpreted as the mirror-frequency coupling (MFC) effect in [19]. For a single-phase VSC, the number of coupled frequencies is conceptually infinite [16], due to the time-periodic nature of the system. It is also noticed that using the harmonic linearization method to obtain the VSC impedance exhibiting a large number of frequency couplings is cumbersome to some extent. Instead, the LTP framework-based methods, e.g., harmonic-state-space (HSS) [20] or the harmonic-transfer-function (HTF) [21] method is more feasible for the impedance modeling of such systems. This is because the process of transforming an LTP system from time- to frequency-domain is well-defined and the frequency couplings are inherently accounted in that process. Examples of applying the HSS in the harmonic stability

This work was supported by Norwegian University of Science and Technology (NTNU) under the grant NTNU Energy (81617922).

C. Zhang, M. Molinas are with the Department of Engineering Cybernetics, NTNU, 7034, Trondheim, Norway (email: chen.zhang@ntnu.no; marta.molinas@ntnu.no).

Sjur Føyen is with the Department of Electric Power Engineering, NTNU, 7034, Trondheim, Norway, email: foyen.sjur@ntnu.no.

J. A. Suul is with SINTEF Energy Research, 7491 Trondheim, Norway and also with the Department of Engineering Cybernetics, NTNU, 7034 Trondheim, Norway (Jon.A.Suul@sintef.no)

T. Isobe is with the Faculty of Pure and Applied Sciences, University of Tsukuba, Ibaraki 305-8573, Japan (email: isobe.takanori.gf@u.tsukuba.ac.jp).

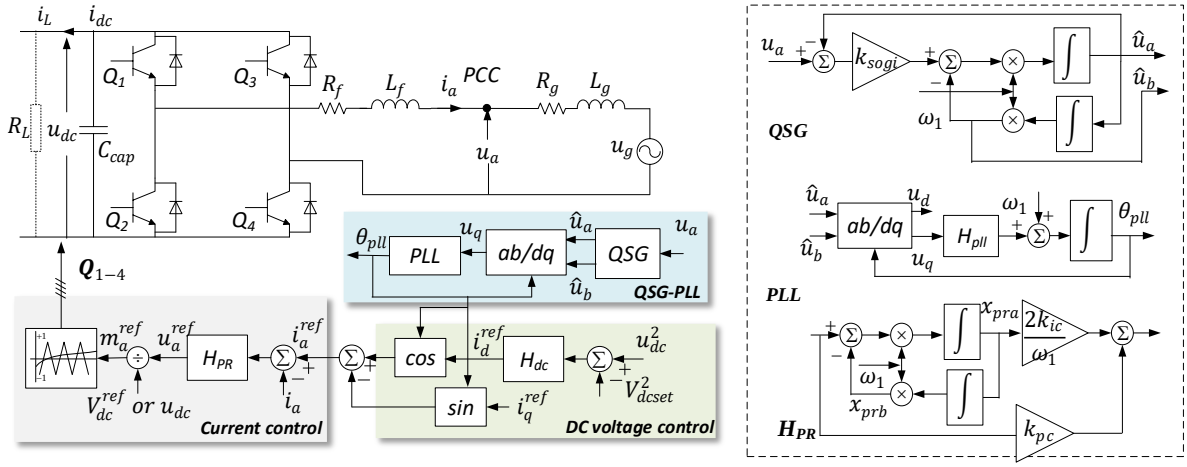

(a) Main circuit and control strategy (b) Control blocks

Fig. 1 Schematic of a typical single-phase grid-VSC system

analysis of a single-phase VSC and a MMC are for instance presented in [22]-[25]. Besides, it is noticed that although this HSS/HTF method can model an LTP system and the frequency characteristic systematically, the resulting impedance is usually a large dimensional matrix representing a multi-input multi-output (MIMO) system. This brings significant challenges in impedance measurement and impedance-based analysis, thus feasible simplification is desired, e.g., exclude the frequency components that are insignificant for impedance modeling.

Relevant analyses with respect to the single-phase VSCs are introduced in [26]-[28]. In which, development of these impedance models is commonly based on the assumption that the steady-state harmonics in the system are negligible, this simplification brings two effects: the number of frequency coupling for impedance modeling is drastically reduced, and the approximate system is LTI so that the conventional time to frequency-domain transformation can be applied for impedance extraction. Based on a similar assumption, [14] and [29] developed the sequence impedance of a single-phase VSC by means of harmonic linearization. Basically, the above impedance models regardless of modeling domains are characterized by a 2-by-2 matrix which can primarily capture the MFC effect with the single-phase VSC system. A latest work in [30] extends the model into a 3-by-3 matrix being able to capture more frequency components so that the model accuracy is improved. It can be obtained that the more frequency components considered in the modeling process, the more accurate the resulting model. However, here lacks a model comparison and a clarification on how many frequency components should be considered for modeling.

To fulfill such a study, or more generally to facilitate better impedance-based analyses, the MIMO impedance obtained from the HSS/HTF is not a desirable choice, thus it would be of significant importance to developing a simple and high-fidelity model that can simplify the impedance-based analysis.

To fill this gap, this paper presents a single-input and single-output (SISO) equivalent modeling technique for the impedance modeling and analysis of the single-phase grid-connected VSC. Based on this SISO modeling technique, this paper further clarifies the accuracy of several reduced-order VSC impedance models obtained from different truncations of the HTF-based model and discusses the stability impacts of the VSC controls with and without compensating the dc voltage variation. These studies also demonstrate how the proposed SISO modeling technique facilitates a simpler and more practically applicable impedance-based analysis.

II. Harmonic Domain Impedance Modeling and Analysis of the Single-phase Grid-VSC System

A. Study system

Fig. 1 depicts a typical single-phase grid-VSC system composed of a full-bridge VSC, an *L*-type filter, a resistive dc load, and a Thevenin equivalent grid. The outer-loop controls the average value of the squared dc voltage using a proportional-integral (PI) regulator while the inner-loop controls the ac current using a proportional-resonant (PR) regulator. The grid-synchronization is fulfilled by a quadrature-signal-generator (QSG) based on a Second Order Generalized Integrator (SOGI) and a conventional phase-locked-loop (PLL).

As also indicated in the lower left of Fig. 1, two approaches for calculating the modulation index m_a^{ref} are considered:

$$\begin{cases} m_{\mathrm{a}}^{\mathrm{DM}} = u_{\mathrm{a}}^{\mathrm{ref}} / V_{\mathrm{dc}}^{\mathrm{ref}} \\ m_{\mathrm{a}}^{\mathrm{CM}} = u_{\mathrm{a}}^{\mathrm{ref}} / u_{\mathrm{dc}} \end{cases} \tag{1}$$

where $m_{\mathrm{a}}^{\mathrm{DM}}$ obtained with a constant dc voltage $V_{\mathrm{dc}}^{\mathrm{ref}}$ is referred to as the Direct Modulation (DM) case in this paper; and $m_{\mathrm{a}}^{\mathrm{CM}}$ obtained with an instantaneous dc voltage u_{dc} is referred to as the Compensated Modulation (CM) case. In addition, the CM usually has better power quality than the DM [31]. In this paper, the CM and DM cases are used mainly because they represent two different operating conditions for steady-state harmonics without introducing too many differences in control systems. Thus, they are useful examples not only for illustrating the application of the proposed SISO equivalent modeling, but also for evaluating the impacts of steady-state harmonics on the extent of frequency couplings, model reduction, and small-signal stability.

B. Modeling conventions

For an LTI element, e.g. the dc voltage controller $H_{\mathrm{dc}}(s) = k_{\mathrm{pdc}} + \frac{k_{\mathrm{idc}}}{s}$, its harmonic domain model (i.e. the HTF) is composed of the frequency-shifted copies of $H_{\mathrm{dc}}(s)$ [21]:

$$\boldsymbol{H}_{\mathrm{dc}}(s) = diag\left(\cdots, H_{\mathrm{dc}}(s-\mathrm{j}\omega_1), H_{\mathrm{dc}}(s), H_{\mathrm{dc}}(s+\mathrm{j}\omega_1), \cdots\right) \quad (2)$$

For brevity, in the later analysis, the notation $H_{\mathrm{dc}(k)}(s)$ will be adopted for representing the component $H_{\mathrm{dc}}(s+k\cdot\mathrm{j}\omega_1)$ and the Laplace variable in $H_{\mathrm{dc}(k)}(s)$ is often omitted.

For an LTP element as A(t), its harmonic domain model is a Toeplitz matrix [20] ($P\{\}$ is the Toeplitz operator):

$$P\{A(t)\} = \begin{bmatrix} \ddots & \ddots & \ddots & & \\ \ddots & A_0 & A_{-1} & A_{-2} & \\ \ddots & A_{+1} & A_0 & A_{-1} & \ddots \\ & A_{+2} & A_{+1} & A_0 & \ddots \\ & & \ddots & \ddots & \ddots \end{bmatrix} \quad (3)$$

in which $A_{\pm k}$ is the $\pm k$ th Fourier coefficient of A(t).

In general, the harmonic-domain models of the VSC and grid are derived according to the following steps: i) perform the linearization on system blocks; ii) transform the linearized blocks into the harmonic domain; iii) formulate the harmonic domain impedance/admittance using the transformed blocks in conjunction with circuit and control diagrams. In later analysis, these steps are applied without any further detailed discussions.

C. Harmonic domain models of the grid-VSC system

1) The VSC harmonic-domain admittance

Based on the above-mentioned modeling process, the VSC harmonic domain admittance defined as

$$-\Delta\boldsymbol{I}_{\mathrm{a}}(s) = \boldsymbol{Y}_{\mathrm{c}}^{\mathrm{HTF}}(s)\cdot\Delta\boldsymbol{U}_{\mathrm{a}}(s) \quad (4)$$

can be derived, where $\boldsymbol{Y}_{\mathrm{c}}^{\mathrm{HTF}}(s)$ is given in (5). By setting the parameters $\boldsymbol{K}_1$ and $\boldsymbol{K}_2$ in (5) as:

$$\begin{aligned} &\mathrm{CM}: \boldsymbol{K}_1 = \boldsymbol{U}_{\mathrm{dc0}}^{-1}, \boldsymbol{K}_2 = \boldsymbol{M}_0^{\mathrm{ref}} \\ &\mathrm{DM}: \boldsymbol{K}_1 = 1/V_{\mathrm{dc}}^{\mathrm{ref}}, \boldsymbol{K}_2 = \boldsymbol{0} \end{aligned} \quad (6)$$

admittance under the CM or the DM case can be determined. The detailed steps required for the harmonic domain modeling of the studied system are presented in Appendix A.

2) The grid harmonic-domain impedance

The grid harmonic-domain impedance of this study is straightforward which is

$$\boldsymbol{Z}_{\mathrm{g}}^{\mathrm{HTF}}(s) = diag\left(\cdots, Z_{\mathrm{g}(-1)}(s), Z_{\mathrm{g}(0)}(s), Z_{\mathrm{g}(+1)}(s), \cdots\right) \quad (7)$$

where $\boldsymbol{Z}_{\mathrm{g}}^{\mathrm{HTF}}(s)$ contains the frequency-shifted copies of $Z_{\mathrm{g}(0)}(s)$ and $Z_{\mathrm{g}(0)}(s) = R_g + sL_g$.

D. HTF truncation and VSC-MIMO admittance analysis

Practically, the truncated version of $\boldsymbol{Y}_{\mathrm{c}}^{\mathrm{HTF}}(s)$ and $\boldsymbol{Z}_{\mathrm{g}}^{\mathrm{HTF}}(s)$ are adopted for numerical analysis. If the HTFs are truncated to a harmonic-order of N, they can be generally represented by a $(2N+1)$-by-$(2N+1)$ dimensional matrix as (8). In later analysis, the truncated VSC-HTF and grid-HTF model are denoted by the *VSC-MIMO admittance* (e.g. $\boldsymbol{Y}_{\mathrm{c}}^{\mathrm{N\times N}}(s)$) and the *grid-MIMO impedance* (e.g. $\boldsymbol{Z}_{\mathrm{g}}^{\mathrm{N\times N}}(s)$).

$$\boldsymbol{H}^{\mathrm{N\times N}}(s) = \begin{bmatrix} H_{(0)}(s-\mathrm{j}N\omega_1) & \cdots & H_{(-N)}(s) & \cdots & H_{(-2N)}(s+\mathrm{j}N\omega_1) \\ \vdots & \ddots & \vdots & \ddots & \vdots \\ H_{\mathrm{N}}(s-\mathrm{j}N\omega_1) & \ddots & H_{(0)}(s) & \ddots & H_{(\mathrm{N})}(s+\mathrm{j}N\omega_1) \\ \vdots & \ddots & \vdots & \ddots & \vdots \\ H_{(2N)}(s-\mathrm{j}N\omega_1) & \cdots & H_{(+N)}(s) & \cdots & H_{(0)}(s+\mathrm{j}N\omega) \end{bmatrix} \quad (8)$$

The choice of harmonic-order N for truncation is important for model accuracy. Prior knowledge regarding the number of dominant frequency couplings in the system is helpful. In this regard, it is already noticed that the MFC effect (i.e. $\pm f_p$ and $\mp f_p + 2f_1$) due to *dq* asymmetry of VSC controls (e.g. PLL) are dominant components for balanced three-phase VSCs. As for the single-phase VSC, qualitatively, due to the ac/dc modulation process, the frequency response will at least contain components: $\pm f_p$ and $\pm f_p \pm 2f_1$, thus at least $N = \pm 2$ should be selected for HTF truncation. Different from the MFC in three-phase VSC, frequency responses at $\pm f_p \pm 2f_1$ are not only related to *dq* asymmetry of VSC controls but also affected by the 2nd harmonic in the dc voltage. In addition, the triple harmonic on the ac-side could also be relevant for modeling. Therefore, in this paper, $N = \pm 3$ is selected for truncation and the resulting VSC-MIMO admittance is denoted by $\boldsymbol{Y}_{\mathrm{c}}^{7\times 7}(s)$.

To better visualize the frequency coupling effect, the VSC-MIMO admittance $\boldsymbol{Y}_{\mathrm{c}}^{7\times 7}(s)$ under both the CM and DM case will be plotted together with the measured frequency response from PSCAD/EMTDC (main parameters are listed in Table I). Due to the limited space, only the magnitude response is shown, and the *Y*-axes of subfigures are scaled to an identical range $[10^{-3}, 10^{-1}]$ to highlight the dominant components.

As shown in Fig. 2 (a), magnitude responses under either of the cases are primarily located at the diagonals $Y_{\mathrm{c}(k)}^{7\times 7}, k = 0, \pm 2, \pm 4$ (the subscript k denotes the element in (8)) since other responses present null values in the defined scale. Also, for each two of adjacent diagonals, they are separated by $2\omega_1$, which means the frequency couplings existent in this

$$\boldsymbol{Y}_{\mathrm{c}}^{\mathrm{HTF}}(s) = -\boldsymbol{C}_{\mathrm{i}}\begin{bmatrix} s\boldsymbol{I} + \boldsymbol{N}_{\mathrm{blk}} - \boldsymbol{A}_{\mathrm{c}} - \\ \boldsymbol{B}_{\mathrm{m}}\boldsymbol{G}_{\mathrm{del}}\boldsymbol{K}_1\left[2\boldsymbol{H}_{\mathrm{PR}}\boldsymbol{A}_{\cos}(\delta_{\mathrm{pll0}})\boldsymbol{H}_{\mathrm{dc}}\boldsymbol{U}_{\mathrm{dc0}} - \boldsymbol{K}_2 \quad -\boldsymbol{H}_{\mathrm{PR}}\right]\begin{bmatrix}\boldsymbol{C}_{\mathrm{dc}} \\ \boldsymbol{C}_{\mathrm{i}}\end{bmatrix} \end{bmatrix}^{-1}\left(\boldsymbol{B}_{\mathrm{u}} - \boldsymbol{B}_{\mathrm{m}}\boldsymbol{G}_{\mathrm{del}}\boldsymbol{U}_{\mathrm{dc0}}^{-1}\boldsymbol{H}_{\mathrm{PR}}\boldsymbol{I}_{\mathrm{b0}}^{\mathrm{ref}}\boldsymbol{G}_{\theta\_\mathrm{u}}\right) \quad (5)$$

TABLE I MAIN CIRCUIT AND CONTROL PARAMETERS

Circuit parameters		Control parameters
U_N = 200 V(rms)	L_g = 6.6 mH	H_{PLL}: k_{ppll} = 0.1, k_{ipll} = 100
I_N = 7 A (rms)	R_g = 0.258 ohm	H_{PR}: k_{pc} = 20, k_{ic} = 628
L_f = 3.3 mH	C_{cap} = 200 uF	H_{dc}: k_{pdc} = 5*10^{-5}, k_{idc} = 2.5*10^{-4}
R_f = 0.129 ohm	V_{dcN} = 320 V	k_{QSG} = 5.0
f_{sw} = 10 kHz	f_{sample} = 50 kHz	T_d = 50 us

system is primarily related to components at $\pm f_k$ and $\pm f_k \pm 2f_1$, where $f_k = f_p + kf_1$ are the shifted copies of f_p. This observation justifies the aforementioned dominant frequency components in the system. Besides, responses away from the central diagonal gradually reduce, e.g., components in $Y_{c(\pm4)}^{7\times7}$ are much smaller than those in $Y_{c(\pm0)}^{7\times7}$. On the other hand, magnitude responses under the CM case are different from those under the DM case, see Fig. 2 (b), in particular, the differences are evident for components away from the central diagonal. This analysis implies that a smaller steady-state harmonic can bring a lower extent of frequency couplings.

Overall, this VSC-MIMO admittance analysis indicates that i) the order of this VSC-MIMO admittance ($N = \pm3$) can be further reduced since the magnitude responses away from the central diagonal are decaying in a great extent; ii) characteristics of the VSC-MIMO admittance under the CM and DM case are not the same which implies that the impacts

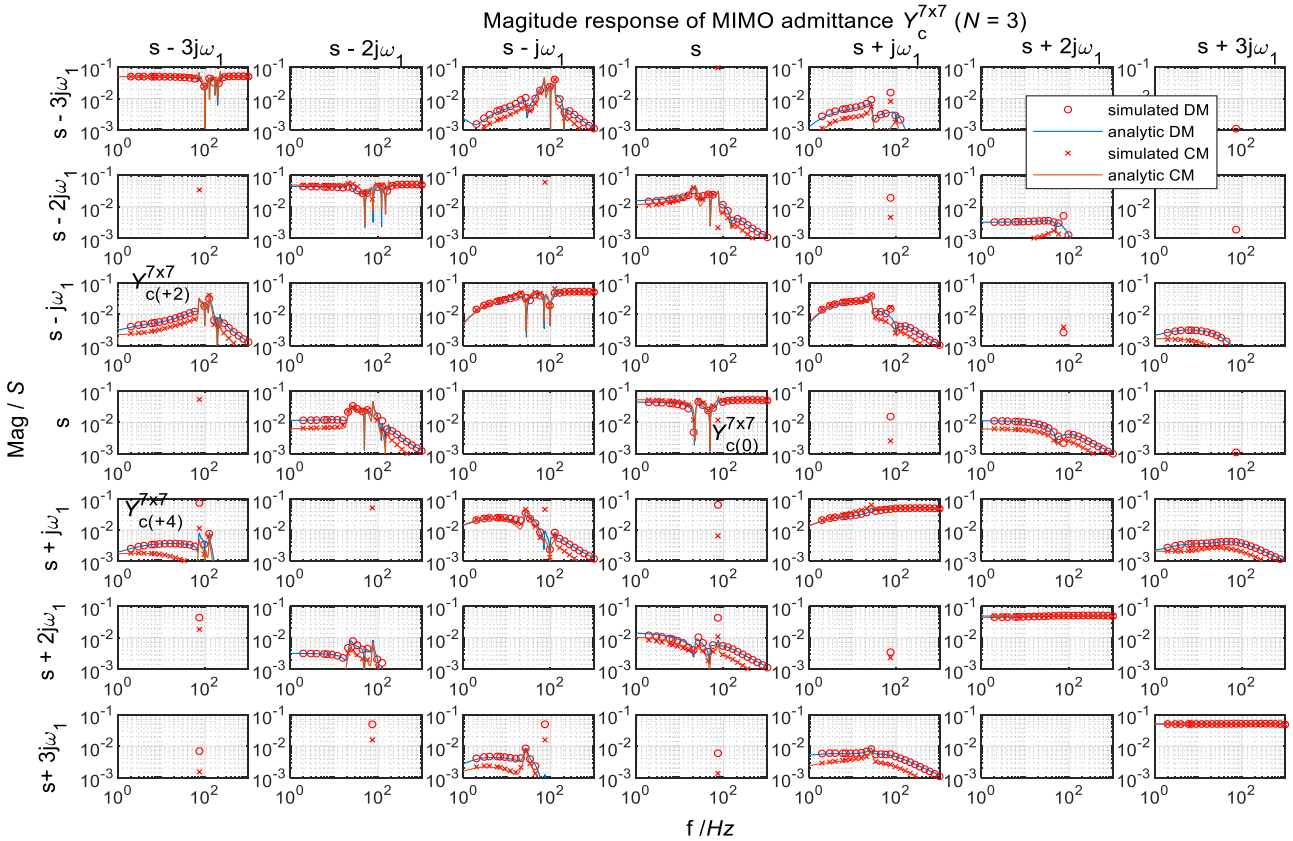

(a) VSC-MIMO admittance plot

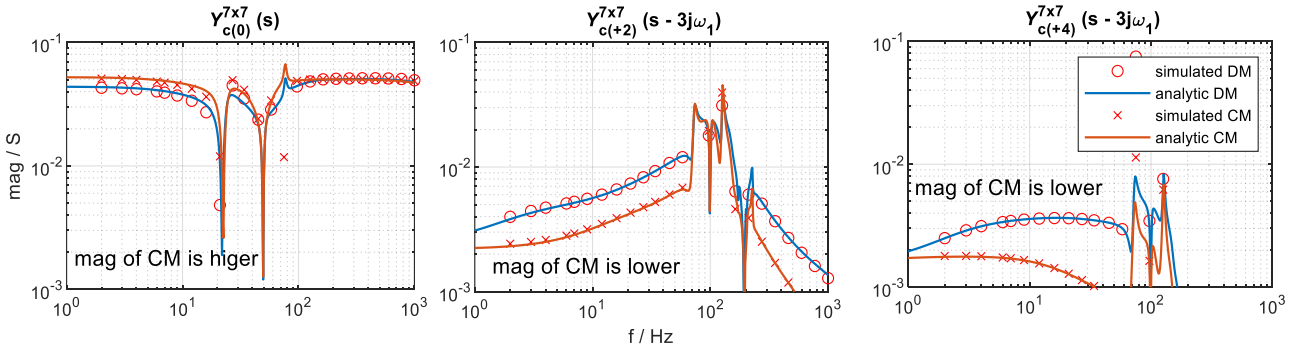

(b) Zoomed in plots of the extracted three components

Fig. 2 Magnitude responses of the VSC-MIMO admittance ($N = \pm3$ and $I_q^{ref} = -3\ A, R_L = 1e5\ ohm$)

on model simplification are expected. These two main findings will be discussed more in detail after the introduction of the SISO equivalent modeling techniques.

III. SISO Equivalent Modeling Technique and Comparative Analysis of VSC Reduced-order Models

The developed VSC-MIMO admittance $\boldsymbol{Y}_{\mathrm{c}}^{7\times7}(s)$ is rather complicated to analyze and implement due to the large model dimension. For instance, to measure this 7-by-7 matrix, seven independent perturbations should be used at each frequency point which is cumbersome for frequency-sweeping. In regard to stability analysis, although the generalized Nyquist criterion (GNC) can be used [32], stability assessment is not intuitive due to the presence of multiple eigenloci. All these arguments point to the benefits of using a SISO model.

The most simplified SISO model is the component $Y_{\mathrm{c}(0)}^{7\times7}(s)$ in $\boldsymbol{Y}_{\mathrm{c}}^{7\times7}(s)$. Clearly, this SISO model ignores all the frequency coupling effects and may not be useful for analysis. In order to preserve the frequency couplings while using the SISO representation, authors in [33] introduced an equivalent SISO modeling by viewing the grid and VSC as a closed-loop system. Inheriting this spirit, this section will present the SISO equivalent modeling technique applied to the harmonic domain.

A. Principle of the MIMO to SISO conversion

In essence, the previously derived VSC and grid MIMO models (i.e. $\boldsymbol{Y}_{\mathrm{c}}^{\mathrm{N\times N}}(s)$ and $\boldsymbol{Z}_{\mathrm{g}}^{\mathrm{N\times N}}(s)$) are defined in an open-loop sense. When they are connected, they will form a closed-system and interactions will occur among them. As illustrated in Fig. 3 (a), if the VSC is perturbed at ω_p by an independent voltage source, the current responses will not only contain the component at ω_p but also contain harmonics at $\omega_p + k\omega_1, k = \pm1 \ldots \pm N$ according to $\boldsymbol{Y}_{\mathrm{c}}^{\mathrm{N\times N}}(s)$. When flowing through the grid impedance $\boldsymbol{Z}_{\mathrm{g}}^{\mathrm{N\times N}}(s)$, the current responses of the VSC will induce harmonics voltages at the grid-side as $\boldsymbol{U}_{\mathrm{g(k)}}(\omega_{\mathrm{p}}), k = 0, \pm1, .., \pm N$. Also, since there is only one independent source $\boldsymbol{U}_{ptb}(\omega_p)$ in the circuit, the harmonic voltages of the VSC and grid must comply with $\boldsymbol{U}_{g(\pm k)}(\omega_p) = \boldsymbol{U}_{a(\pm k)}(\omega_p), k \neq 0$, which means they are mutually dependent.

From the above illustration and Fig. 3 it can be found that viewing the grid-VSC as a closed-loop system, the dependent paths can be eliminated from circuit operations. From which, an equivalent relation of the input-voltage and output-current under the same frequency ω_{p} is established, which corresponds to the SISO equivalent model of this paper.

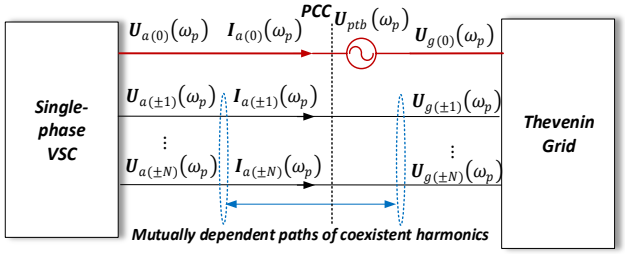

(a) Circuit illustration of the harmonic interactions

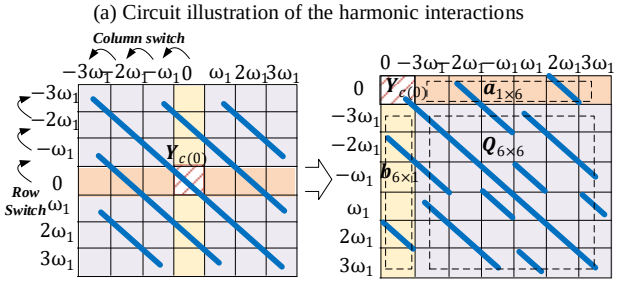

(b) Illustration of the matrix rearrangement

Fig. 3 The principle and method of MIMO to SISO conversion

B. Method for deriving the SISO equivalent model

To make the circuit operations easier, the columns and rows of the $\boldsymbol{Y}_{\mathrm{c}}^{\mathrm{N\times N}}(s)$ and $\boldsymbol{Z}_{\mathrm{g}}^{\mathrm{N\times N}}(s)$ are rearranged so that they can be compactly represented by vectors or sub-matrix blocks. The concept to achieve this rearrangement is shown in Fig. 3 (b), where e.g., the columns and rows of $\boldsymbol{Y}_{\mathrm{c}}^{7\times7}(s)$ are sequentially switched until the component $Y_{\mathrm{c}(0)}^{7\times7}(s)$ is moved to the left-top corner of the matrix.

Thus, for a *N*-order model of the VSC and grid, the following equations can be established

$$-\begin{bmatrix} I_{\mathrm{a}(0)}(s) \\ \boldsymbol{I}_{\mathrm{ah}}(s) \end{bmatrix} = \begin{bmatrix} Y_{\mathrm{c}(0)}^{\mathrm{N\times N}} & \boldsymbol{a}_{1\times2\mathrm{N}} \\ \boldsymbol{b}_{2\mathrm{N}\times1} & \boldsymbol{Q}_{2\mathrm{N}\times2\mathrm{N}} \end{bmatrix} \begin{bmatrix} U_{\mathrm{a}(0)}(s) \\ \boldsymbol{U}_{\mathrm{ah}}(s) \end{bmatrix}$$
$$\begin{bmatrix} U_{\mathrm{g}(0)}(s) \\ \boldsymbol{U}_{\mathrm{ah}}(s) \end{bmatrix} = \begin{bmatrix} Z_{\mathrm{g}(0)}^{\mathrm{N\times N}} & \boldsymbol{0}_{1\times(2\mathrm{N}-1)} \\ \boldsymbol{0}_{(2\mathrm{N}-1)\times1} & \boldsymbol{c}_{2\mathrm{N}\times2\mathrm{N}} \end{bmatrix} \begin{bmatrix} I_{\mathrm{a}(0)}(s) \\ \boldsymbol{I}_{\mathrm{ah}}(s) \end{bmatrix} \quad (9)$$

where $Y_{\mathrm{c}(0)}^{\mathrm{N\times N}}, \boldsymbol{a}_{1\times2\mathrm{N}}, \boldsymbol{b}_{2\mathrm{N}\times1}, \boldsymbol{Q}_{2\mathrm{N}\times2\mathrm{N}}$ are known components that can be extracted from $\boldsymbol{Y}_{\mathrm{c}}^{\mathrm{N\times N}}(s)$. $\boldsymbol{c}_{2\mathrm{N}\times2\mathrm{N}} = \boldsymbol{Z}_{\mathrm{g(k)}}^{\mathrm{N\times N}}, k \neq 0$, $\boldsymbol{I}_{\mathrm{ah}}(s) = \left[I_{\mathrm{a}(-\mathrm{N})}, \ldots, I_{\mathrm{a(k)}}, \ldots, I_{\mathrm{a}(+\mathrm{N})} \right]^T$, and $\boldsymbol{U}_{\mathrm{ah}}(s)\,(k \neq 0)$ has a similar format as $\boldsymbol{I}_{\mathrm{ah}}(s)$.

According to Fig. 3 (a) and (10), there are $2(2N+1)+2$ unknown variables (i.e. $\boldsymbol{U}_{a(\pm k)}, \boldsymbol{I}_{a(\pm k)}, \boldsymbol{U}_{ptb}, \boldsymbol{U}_{g(0)}$) and $2(2N+1)+1$ sets of known equations where one augmented equation that is not shown in (9) but can be derived from Fig. 3 (a) is $\boldsymbol{U}_{ptb} + \boldsymbol{U}_{g(0)} = \boldsymbol{U}_{a(0)}$. Based on this, the relation of $\boldsymbol{U}_{a(0)}$ and $\boldsymbol{I}_{a(0)}$ is can be established which is written as

$$-I_{\mathrm{a}(0)}(s) = \underbrace{\left(Y_{\mathrm{c}(0)}^{\mathrm{N\times N}} - \boldsymbol{a}_{1\times2\mathrm{N}} \left(\boldsymbol{I} + \boldsymbol{c}_{2\mathrm{N}\times2\mathrm{N}} \boldsymbol{Q}_{2\mathrm{N}\times2\mathrm{N}} \right)^{-1} \boldsymbol{c}_{2\mathrm{N}\times2\mathrm{N}} \boldsymbol{b}_{2\mathrm{N}\times1} \right)}_{Y_{\mathrm{c}}^{\mathrm{SISO}}(s)} \cdot U_{\mathrm{a}(0)}(s) \quad (11)$$

and the grid-SISO model is

$$U_{\mathrm{g}(0)}(s) = Z_{\mathrm{g}(0)}^{\mathrm{N\times N}}(s) I_{\mathrm{a}(0)}(s) = Z_{\mathrm{g}}^{\mathrm{SISO}}(s) I_{\mathrm{a}(0)}(s) \quad (12)$$

It can be seen that the derived VSC-SISO admittance $Y_{\mathrm{c}}^{\mathrm{SISO}}(s)$ is composed of two terms, the first term $Y_{\mathrm{c}(0)}^{\mathrm{N\times N}}$

reflects the relation of input and output at the same frequency while the second-term reflects the effects of the harmonic interactions between the grid and the VSC. Furthermore, when the Nyquist-based stability analysis is performed, it has been proven in [33] that the SISO equivalent system has an identical critical stability condition to that of the original MIMO system (A similar proof based on a simplified representation of the cases studied is presented in Appendix. B). Therefore, the presented SISO equivalent modeling technique itself will not compromise the accuracy in analysis.

C. Comparative analysis of the VSC full- and reduced-order admittances by using the SISO modeling technique

Based on the above method, VSC reduced-order models from different truncations of $\boldsymbol{Y}_{\mathrm{c}}^{7\times7}(s)$ can be effectively compared via their SISO equivalents. In Fig. 4, the following VSC models of different orders are considered for comparison:

1) the *full-order model* uses all the components of $\boldsymbol{Y}_{\mathrm{c}}^{7\times7}(s)$

2) the reduced-order *Model 1* directly uses the component $Y_{\mathrm{c}(0)}^{7\times7}(s)$ of $\boldsymbol{Y}_{\mathrm{c}}^{7\times7}(s)$, thus this is a scalar model;

3) the reduced-order *Model.2* extracts the frequency components f_p and f_p+2f_1 from $\boldsymbol{Y}_{\mathrm{c}}^{7\times7}(s)$, thus it is a 2x2 matrix model and resembles the ones in [26]-[29];

4) the reduced-order *Model.3* extracts the frequency components f_p and $f_p\pm2f_1$ from $\boldsymbol{Y}_{\mathrm{c}}^{7\times7}(s)$, thus it is a 3-by-3 matrix model and resembles the one in [30]. Notations of corresponding SISO equivalent models are listed in Table II.

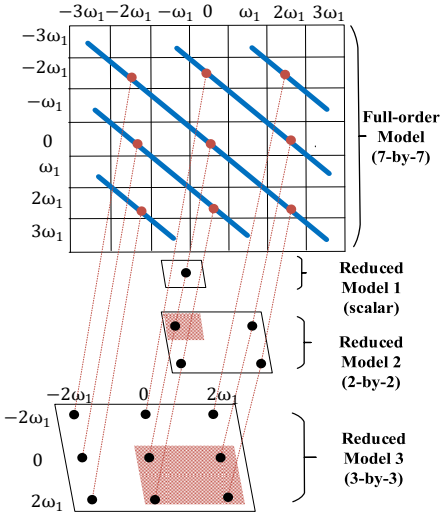

Fig. 4 Extraction of the reduced VSC-MIMO admittances

TABLE II NOTATIONS OF DIFFERENT SISO EQUIVALENTS

Name	MIMO model dimension	SISO model notation
Full-order model	7x7	$Y_{\mathrm{c\_full}}^{\mathrm{SISO}}$
Reduced-order model 1	scalar	$Y_{\mathrm{c\_rm1}}^{\mathrm{SISO}}$
Reduced-order model 2	2x2	$Y_{\mathrm{c\_rm2}}^{\mathrm{SISO}}$
Reduced-order model 3	3x3	$Y_{\mathrm{c\_rm3}}^{\mathrm{SISO}}$

In order to test these models under a relatively critical condition, i.e., low stability margin, the current controller gain is reduced while the dc voltage controller gain is increased. Similar conditions with low stability margin state can occur in practical situations, e.g. for operation in weak AC grids.

According to the comparative results in Fig. 5, the SISO model $Y_{\mathrm{c\_full}}^{\mathrm{SISO}}$ converted from the full-order MIMO model is consistent with measurements and is accurate under both the CM and DM cases. Thus, $Y_{\mathrm{c\_full}}^{\mathrm{SISO}}$ will be served as the reference model for later comparisons.

The model accuracy of different truncations under the DM case is compared and shown in Fig. 5 (a). The accuracies of the reduced-order VSC models, if ranked in a descending sequence, is given by $Y_{\mathrm{c\_rm3}}^{\mathrm{SISO}} > Y_{\mathrm{c\_rm2}}^{\mathrm{SISO}} > Y_{\mathrm{c\_rm1}}^{\mathrm{SISO}}$. From the plots, it can be seen that $Y_{\mathrm{c\_rm3}}^{\mathrm{SISO}}$ only has small differences from $Y_{\mathrm{c\_full}}^{\mathrm{SISO}}$ under this DM case. Thus, its accuracy is defined as: *High*. Besides, $Y_{\mathrm{c\_rm2}}^{\mathrm{SISO}}$ exhibits evident discrepancies from $Y_{\mathrm{c\_full}}^{\mathrm{SISO}}$, thus its accuracy is defined as: *Medium* (−), whereas $Y_{\mathrm{c\_rm1}}^{\mathrm{SISO}}$ is defined as *Low* if compared to the accuracy of $Y_{\mathrm{c\_rm2}}^{\mathrm{SISO}}$.

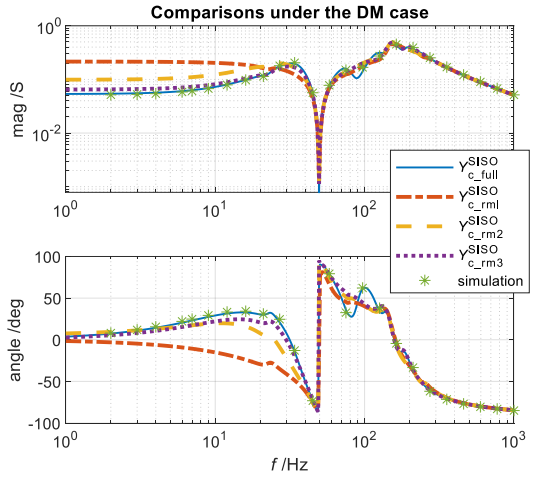

(a) Comparisons under the DM case

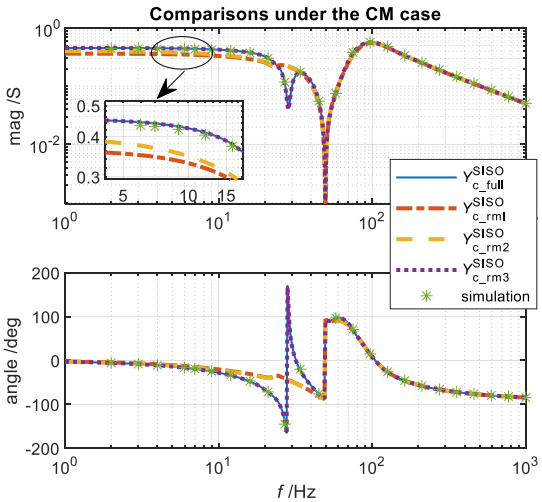

(b) Comparisons under the CM case

Fig. 5 SISO equivalents-based comparative analysis of reduced-order VSC admittances (k_{pc} = 2, dc voltage control gain is doubled, $I_q^{ref} = -3\ A, R_L = 1e5\ ohm$, other configurations are identical to Table I)

Next, model accuracies under the CM case are compared and shown in Fig. 5 (b). Overall, the model accuracies of reduced-order VSC models are improved compared to the DM case. In detail, $Y_{c\_rm3}^{SISO}$ is as accurate as $Y_{c\_full}^{SISO}$ under this CM case Furthermore, $Y_{c\_rm1}^{SISO}$ and $Y_{c\_rm2}^{SISO}$ are almost close to $Y_{c\_full}^{SISO}$ in terms of admittance shapes although one of the resonances is mispredicted. Also, it is noted that the differences between $Y_{c\_rm2}^{SISO}$ and $Y_{c\_rm1}^{SISO}$ are very small though $Y_{c\_rm2}^{SISO}$ turns out to be slightly more accurate (as can be seen from the zoom-in subfigure), thus their accuracies are defined as: Medium (−) and Medium (+) respectively. A summary of this analysis is shown in Table III.

TABLE III SUMMARY OF THE MODEL REDUCTION ANALYSIS

Name	SISO model notation	Accuracy DM case	Accuracy CM case
Full-order model	$Y_{c\_full}^{SISO}$	Accurate	Accurate
Reduced-order model 1	$Y_{c\_rm1}^{SISO}$	Low	Medium
Reduced-order model 2	$Y_{c\_rm2}^{SISO}$	Medium (−)	Medium (+)
Reduced-order model 3	$Y_{c\_rm3}^{SISO}$	High	Accurate

IV. COMPARATIVE STABILITY ANALYSIS OF THE CM AND DM CASES BY USING THE SISO IMPEDANCES

The previous analysis has shown that reduced-order models exhibit different accuracies under the CM and DM case. This implies that stability differences may also exist, which is interesting to investigate. In this section, the effect of the CM in comparison with the DM case will be analyzed through the full-order SISO impedance $Y_{c\_full}^{SISO}$.

A. Qualitative analysis of the CM effect

According to the harmonic domain modeling presented in Appendix A, the overall system can be represented by Fig. 6. It can be seen that the main model difference between the CM and the DM lies in the parameters $\boldsymbol{K}_1$ and $\boldsymbol{K}_2$, where $\boldsymbol{K}_1 = \boldsymbol{U}_{dc0}^{-1}$, $\boldsymbol{K}_2 = \boldsymbol{M}_{a0}^{ref}$ for the CM case and $\boldsymbol{K}_1 = 1/V_{dc}^{ref}$, $\boldsymbol{K}_2 = \boldsymbol{0}$ for the DC case according to (6).

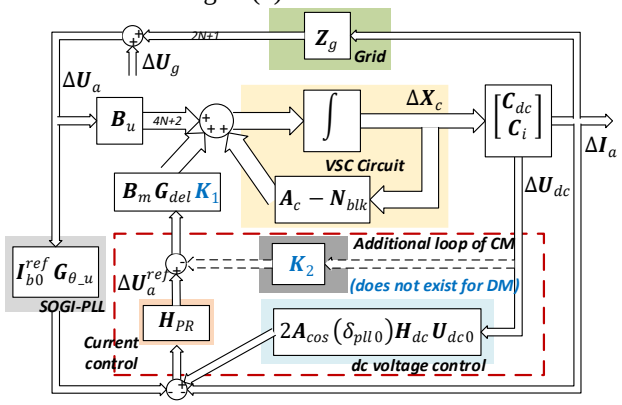

Fig. 6 Harmonic-domain control diagram of the single-phase grid-VSC system

Further, if $\boldsymbol{M}_{a0}^{ref} = \boldsymbol{0}$ holds true, then the CM model and DM model will be approximately the same. However, this condition is barely valid since the VSC needs to output an AC voltage that is comparable to the grid, i.e. $\boldsymbol{M}_{a0}^{ref} \neq \boldsymbol{0}$. This means, the model difference always exists, and this difference is reflected in the additional feedback loop gain $\boldsymbol{M}_{a0}^{ref}$ of the CM case. This gain effect can also be physically interpreted as a sort of damping to the VSC circuit, while the sign of this damping yet remains to be determined.

To evaluate the additional damping characteristic present in the CM model (i.e. positive or negative), a straightforward way is to change $\boldsymbol{M}_{a0}^{ref}$ and see how it shapes the admittance. However, $\boldsymbol{M}_{a0}^{ref}$ cannot be operated directly since it is not an independent control variable.

To overcome this issue, the gain of the parallel control loop can be changed instead, and the resulting effect will be approximately the same as changing the gain of $\boldsymbol{M}_{a0}^{ref}$. For instance, the effect of increasing the gain $\boldsymbol{M}_{a0}^{ref}$ can be qualitatively studied by reducing the parallel control loop gain, where the latter one can be readily fulfilled by reducing the current controller gain.

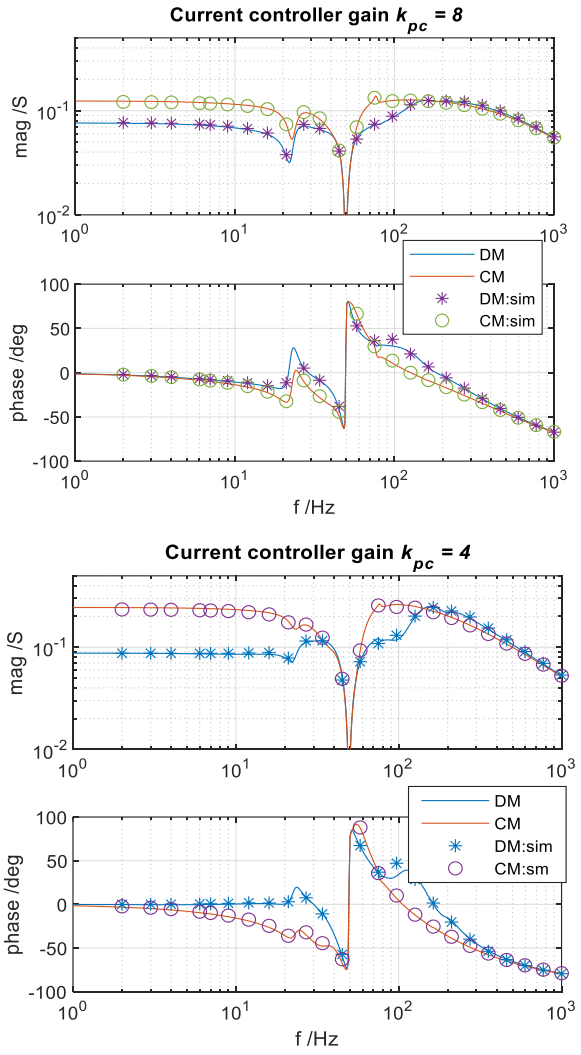

Fig. 7 VSC-SIO admittance comparisons of the CM and DM case ($I_q^{ref} = -3\ A, R_L = 1e5\ ohm$, other configurations in Table I remain unchanged)

B. Negative damping characteristic of the CM effect

Based on the above method, $Y_{c\_full}^{SISO}$ under two types of current controller gains are compared to identify the damping characteristic. As can be seen from Fig. 7, overall, the VSC-SISO admittance under the CM case has higher magnitudes

than those of the DM case. From the impedance-based analysis perspective, it can be obtained that a larger VSC admittance will result in a larger impedance-ratio so that the stability margin is lowered. This implies that the CM case is less stable than the DM case, and thus this additional damping effect presented in the CM case is expected to be negative.

To further study the incremental effect of $\boldsymbol{M}_{a0}^{ref}$ to the CM model itself, the VSC-SISO admittances of the CM case, under k_{pc} = 8 and k_{pc} =4 can be compared. It can be seen that the magnitude response is increased as the current controller gain is reduced, thus a lower stability margin is anticipated. This observation in combination with the previous interpretation that the effect of reducing the current controller gain is equivalent to the effect of increasing $\boldsymbol{M}_{a0}^{ref}$, indicates that this incremental effect of $\boldsymbol{M}_{a0}^{ref}$ to the CM model itself is negative. Based on the above two aspects, it can be concluded that this CM gain effect has a negative damping characteristic.

Further, in order to directly study the stability effect, in the following, the Nyquist-based analysis will be performed.

C. Comparative stability analysis of the CM and DM case

A classic source and load system partitioned at the PCC and based on the SISO equivalent models can be established according to [6]. Thus, the impedance ratio of the closed-loop system can be formulated, from which the Nyquist diagram can be drawn. For this study, the impedance-ratio is derived as $L(s) = Y_{c\_full}^{SISO} Z_{g(0)}^{SISO}$.

In Fig. 8 (a), Nyquist plots of the DM and CM case are compared under a smaller current controller gain (i.e. k_{pc} = 1.25), other configurations are identical to Table I. Under such a condition, both the CM and DM case conclude a stable system (there are no right-half-plane poles in this case). However, it is noticed that the stability margin of the CM case is much lower than that of the DM case, justifying the negative damping effect. In fact, the DM case of this study is a marginally stable system since one of its eigenloci is close to the critical point (-1, 0 j) when it crosses the real axis.

To verify the conclusion from the Nyquist-based stability analysis, time-domain simulation in PSCAD/EMTDC is conducted, where the VSC initially operates under the DM case and then it is switched to the CM case at 3.6s. The current response from this simulation is shown in Fig. 8 (b), from which it can be confirmed that the system is marginally stable under the CM case since the current response is weakly damped.

Besides, from the magnified plots it can be observed that the steady-state current waveform of the CM case is much better than the DM case. This is a known benefit of CM. However, as identified in this analysis, the CM will push the system more towards the stability margin. It is worth mentioning that this analysis is conducted in a low-margin state on purpose, where the waveform of the DM case seems not acceptable. However, if the overall system margin is improved, the DM case can also provide decent power quality. Besides, additional features could be included in the control system to improve the stability margin of the CM case.

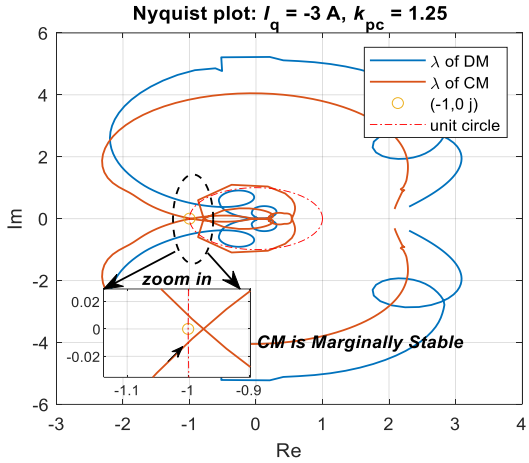

(a) Nyquist plots comparison of the CM and DM case

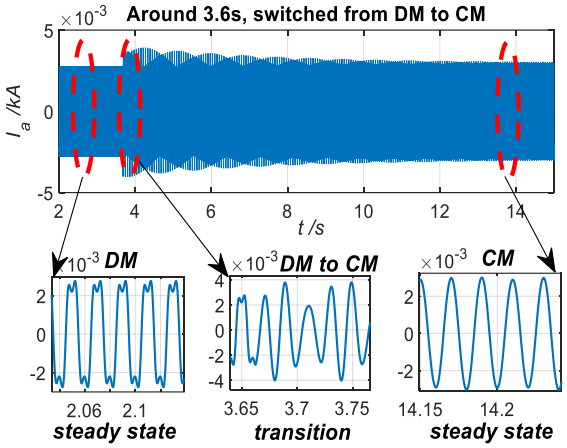

(b) Time-domain ac current waveforms

Fig. 8 Comparative stability analysis and time domain verification of the CM and DM (k_{pc} = 1.25, other parameters are identical to Table I)

V. Experimental Verification

This section presents experimental impedance measurement and verification of the developed full-order VSC-SISO admittance i.e., $Y_{c\_full}^{SISO}$ along with some experimental stability tests to consolidate the theoretical analyses.

A. Experimental setup

The experimental setup is briefly illustrated in Fig. 9 (a), which is composed of a signal generator, an analog superposition circuit, a linear amplifier, a single-phase VSC and an oscilloscope. The VSC control system is implemented in a digital controller based on the PE-expert4 platform, with a control cycle $T_d = 50\ us$.

Regarding the SISO admittance measurement, both the supply voltage and the small-signal perturbation voltage are generated by the signal generator, however, from separate output channels. Thus, an analog circuit in Fig. 9 (a) is used to superpose the signals and send them to the power amplifier, please see the depiction in Fig. 9 (b). The single-tone injection method is applied, which means for a specific time-interval T, only one specified frequency is injected into the system. Then,

this method is repeated for each frequency ranging from 5 Hz to 1 kHz. The time interval T used in this experiment is 6 s to assure the system reaches a good steady-state in this period and to avoid the influence of transients when injecting a new perturbation. Voltage and current data are recorded by the oscilloscope and exported to MATLAB for impedance calculation and analysis (the sampling rate is 50 kHz, and the window for discrete Fourier analysis is 5s).

B. *Experimental verification of the VSC-SISO admittance*

The admittance verification was conducted under both the CM and DM case. Main circuit and control parameters are listed in Table I, and the following two cases are considered:

1) Case I: $I_q^{ref} = -3\ A, R_L = 1e5\ ohm$, i.e. a reactive power load condition.

2) Case II, $I_q^{ref} = 0\ A, R_L = 128\ ohm\ (i.e.\ I_d^{ref} \approx -6\ \mathrm{A})$, i.e. an active power load condition.

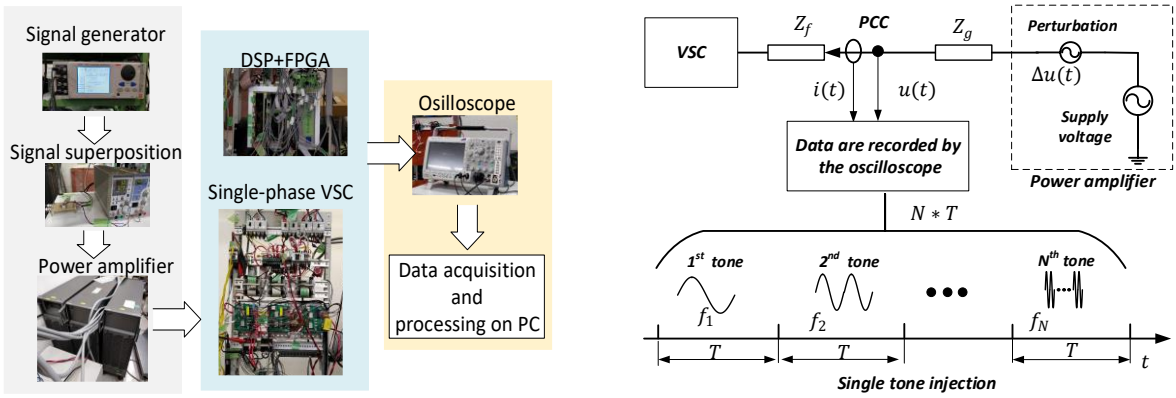

(a) Experimental system layout (b) Illustration of impedance measurement

Fig. 9 Experimental setup for SISO impedance measurement verification

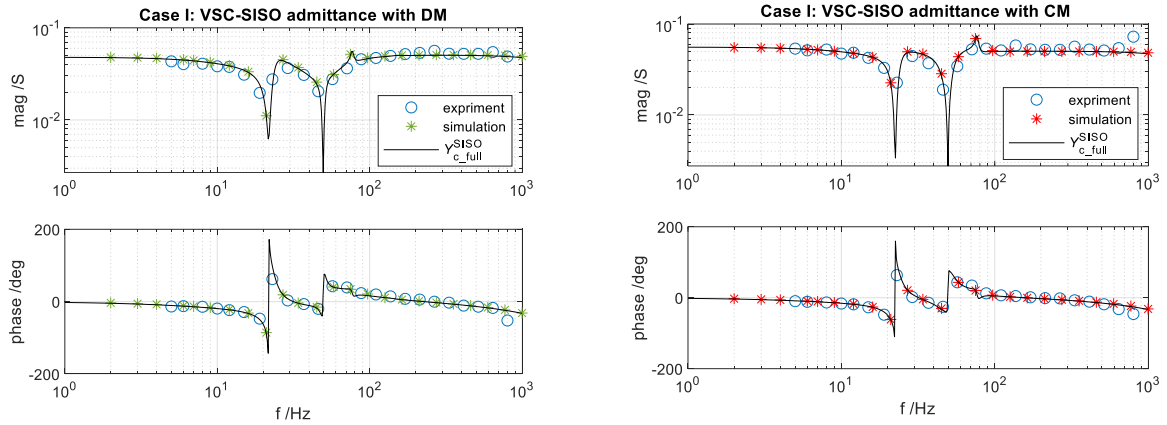

(a) VSC-SISO admittance comparisons under Case I

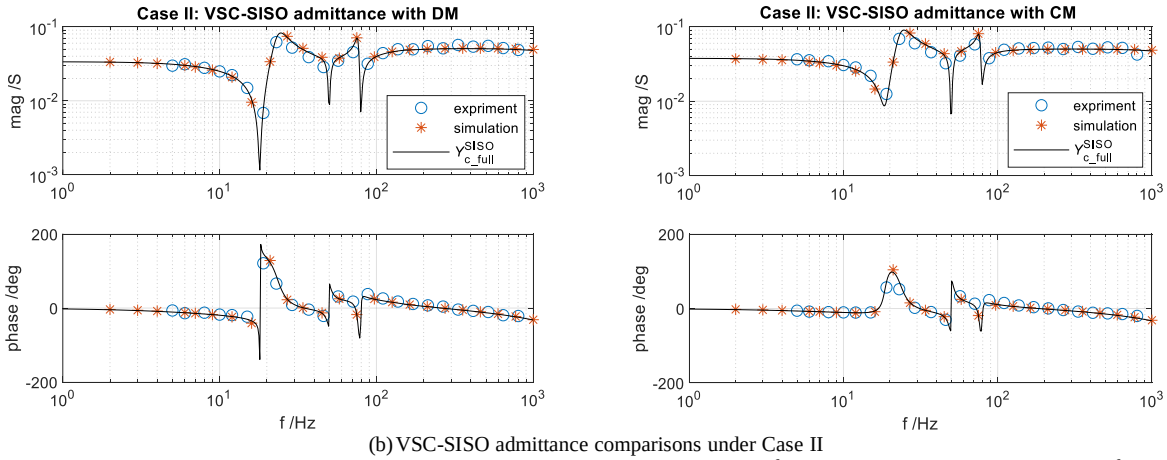

(b) VSC-SISO admittance comparisons under Case II

Fig. 10 Experimental verification of the full-order VSC-SISO admittance model (Case I, $I_q^{ref} = -3\ A, R_L = 1e5\ ohm$; Case II, $I_q^{ref} = 0\ A, R_L = 128\ ohm\ (i.e.\ I_d^{ref} \approx -6\ \mathrm{A})$)

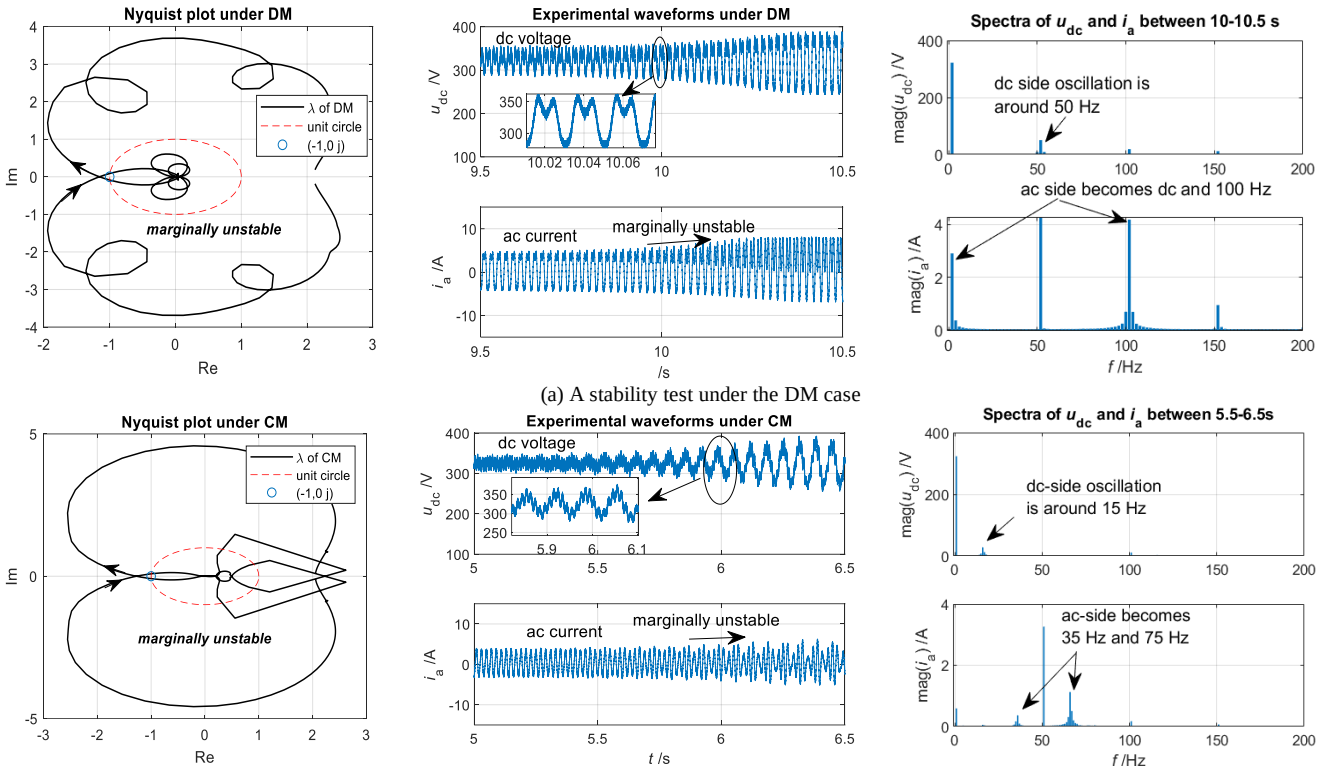

(a) A stability test under the DM case

(b) A stability test under the CM case

Fig. 11 Experimental stability tests under the CM and the DM case

The comparative results are shown in Fig. 10, from which it can be seen that the full-order VSC-SISO admittance $Y_{c\_full}^{SISO}$ is basically consistent with the experimental results for all the scenarios (i.e., under the CM and the DM case, and under different operating points). At the highest frequencies, small deviations between the model and the experiments can be noticed, mainly due to the influence of the sampling effects and frequency- and temperate- dependency of parameters that are not represented in the analytical model. However, a point-to-point match is achieved when compared with the simulated results where the above issues are greatly alleviated. This analysis proves that the developed full-order VSC-SISO admittance $Y_{c\_full}^{SISO}$ is effective and accurate, this also indicates that the MIMO to SISO conversion technique is valid.

Besides, from the comparisons, it can also be noticed that the operating conditions have evident impacts on the admittance characteristics as well.

C. *Experimental stability tests*

This section presents experimental stability tests under both the DM and the CM case along with further justifications on model accuracy and damping analysis. In which, the marginally unstable condition is focused.

Such a condition is achieved by continuously varying the control parameters until the marginally unstable state presents in the Nyquist plot. Corresponding control parameters for the CM and the DM cases are registered and listed in Table IV. Then, these theoretically predicted control parameters will be set in the experimental system seeing if the marginally unstable state will occur or not. It should be noted that, before this change, control parameters in Table I are adopted to assure a stable state.

TABLE IV THEORETICAL PARAMETERS FOR STABILITY TESTS

Parameters	DM case	CM case
H_{PR}	k_{pc} = 2, k_{ic} = 2	k_{pc} = 1, k_{ic} = 2
H_{dc}	k_{pdc} = 5*10^{-5} k_{idc} = 0.05	k_{pdc} = 5*10^{-5} k_{idc} = 2.5*10^{-4}
H_{pll}	k_{ppll} =0.1, k_{ipll} =100	
Load	$I_q^{ref} = -3\,A, R_{load} = 10^5\ ohm$	
Others	The same as Table I	

An experimental stability test under the DM case is first conducted and analyzed. According to the Nyquist plot in Fig. 11 (a), the system will be marginally unstable due to the clockwise encirclement of the critical point (no right-half-plane open-loop poles). Corresponding control parameters are listed in Table IV. After setting these new control parameters to the experimental system around 9.5s, the system gradually becomes oscillatory as can be seen from the time-domain waveforms, proving the Nyquist-based analysis is correct. Also, from the dc voltage and ac current spectra, it can be obtained that the dc-side oscillation frequency of this case study is around 50 Hz, and this oscillation leads to two evidently coupled frequency components on the ac-side, which are at the dc and the 100 Hz. Moreover, the magnitudes of the ac current at these two frequency components are different, implying an asymmetric oscillation similar to the MFC effect of a three-phase VSC.

Next, a similar stability test under the CM case is conducted and the results are shown in Fig. 11 (b). From the Nyquist plot, it is obtained that the system will be marginally unstable due to

the encirclement. This conclusion is justified by the experimental waveforms where instability occurs after the new parameters are set in the experimental system. The dc-side oscillation frequency of this case is around 15 Hz, as a result, the ac side presents two evidently coupled frequency components at 35 Hz and 75 Hz.

The above two stability tests further consolidate the validity of the proposed model and the Nyquist-based analysis. Besides, it is noticed that a simulated stability test under the CM case has been conducted in Fig. 8, where it concludes a marginally stable system with a current controller gain at k_{pc} = 1.25. However, as shown in this experimental stability test in Fig. 11 (b), if the current controller gain is reduced to k_{pc} = 1 while keeping other conditions unchanged from Fig. 8, the system stability condition is changed from marginally stable to marginally unstable. This conclusion confirms again that the additional damping characteristic of the CM case is negative.

VI. Conclusion

This paper presents a SISO equivalent impedance modeling technique that enables a simpler impedance measurement and stability analysis for the single-phase grid-connected VSC. The developed VSC-SISO admittance preserves all the frequency couplings presented in the HTFs, thus they are equivalent in terms of model accuracy. Also, it is noted that since the overall impedance modeling is still based on the principle of switch-average, the resulting model is mainly valid for control-related stability analysis where the frequency-range is far below the switching frequency. For this purpose, the developed VSC-SISO admittance is experimentally verified below 1 kHz.

Applications of the SISO modeling technique for the VSC model reduction and stability characteristic analysis, under the CM and DM cases (i.e. with and without compensating the dc voltage variation in VSC control), are presented. Some main conclusions are listed as follows:

1) Three reduced-order VSC models extracted from its HTF model are compared with respect to model accuracy. The 3-by-3 matrix model characterizing the frequency components f_p, $f_p \pm 2f_1$ is accurate in most cases. The 2-by-2 matrix model characterizing the frequency components f_p, $f_p - 2f_1$ performs decently overall, in particular with relatively small steady-state harmonics (e.g., under the CM case). The scalar model characterizing the frequency component f_p has the lowest accuracy compared to others.

2) In terms of stability, the CM case exhibits an additional negative damping effect to the system compared to the DM case, i.e. the CM case is less stable. Thus, attention should be paid to this unfavorable stability influence from the CM case though it has some benefits in power quality. Ancillary stabilization controls for the CM case are expected to be developed in future works, which can be better fulfilled based on the SISO modeling technique.

At last, although the mathematical development of this SISO equivalent model is rather cumbersome, the process provides insightful evidence on the understanding and the consequences of SISO impedance measurement of an interconnected system with frequency couplings.

Indeed, when measuring the VSC impedance only using the current and voltage at the same frequency, the information of frequency couplings will not be lost as long as such a measurement is conducted in a grid-connected condition. This concept is significantly useful for impedance measurement-based analysis where tedious modeling is not necessary, however, this concept also results in one drawback that the obtained SISO equivalent model is in a closed-loop sense and due to which the VSC-SISO model should always be updated in accordance with the grid conditions.

Appendix

A. Harmonic domain VSC admittance modeling

In the following, the detailed harmonic domain impedance modeling process of the single-phase grid-VSC system as shown in Fig. 1 will be presented.

1) Modeling of the SOGI-QSG PLL

Based on the control blocks in Fig. 1 (b), the HTF of SOGI-based QSG is

$$\begin{bmatrix} \hat{\boldsymbol{U}}_{\mathrm{a}}(s) \\ \hat{\boldsymbol{U}}_{\mathrm{b}}(s) \end{bmatrix} = \begin{bmatrix} \boldsymbol{H}_{\mathrm{QSGa}}(s) \\ \boldsymbol{H}_{\mathrm{QSGb}}(s) \end{bmatrix} \boldsymbol{U}_{\mathrm{a}}(s) \tag{A.1}$$

where $\boldsymbol{H}_{\mathrm{QSGa,b}}$ are composed of the frequency-shifted copies of $H_{\mathrm{QSGa,b}}$; $\boldsymbol{U}_{\mathrm{a,b}}(s) = [..., U_{\mathrm{a,b}(-1)}, U_{\mathrm{a,b}(0)}, U_{\mathrm{a,b}(+1)}, ..]^T$.

Then, the linearized q-axis input of PLL is

$$\Delta u_{\mathrm{q}} = \begin{bmatrix} -\sin\theta_{\mathrm{pll0}}(t) & \cos\theta_{\mathrm{pll0}}(t) \end{bmatrix} \begin{bmatrix} \Delta\hat{u}_{\mathrm{a}} \\ \Delta\hat{u}_{\mathrm{b}} \end{bmatrix} - \hat{U}_{\mathrm{d0}}(t) \cdot \Delta\theta_{\mathrm{pll}} \tag{A.2}$$

where $\theta_{\mathrm{pll0}}(t) = \omega_1 t + \delta_{\mathrm{pll0}}$, $\hat{U}_{\mathrm{d0}}(t)$ is the steady-state d-axis grid voltage estimated by the QSG. Since the SOGI-QSG is very selective, the ac components of $\hat{U}_{\mathrm{d0}}(t)$ will be greatly attenuated, thus $\hat{U}_{\mathrm{d0}}(t) \approx U_{\mathrm{d0}}$ is obtained, where U_{d0} is the dc component. Thus, its HTF model of is

$$\Delta\boldsymbol{U}_{\mathrm{q}}(s) = \begin{bmatrix} -\boldsymbol{A}_{\sin}(\delta_{\mathrm{pll0}}) & \boldsymbol{A}_{\cos}(\delta_{\mathrm{pll0}}) \end{bmatrix} \begin{bmatrix} \Delta\hat{\boldsymbol{U}}_{\mathrm{a}}(s) \\ \Delta\hat{\boldsymbol{U}}_{b}(s) \end{bmatrix} - \boldsymbol{U}_{\mathrm{d0}} \cdot \Delta\boldsymbol{\theta}_{\mathrm{pll}}(s) \tag{A.3}$$

where $\boldsymbol{A}_{\sin}(\delta_{\mathrm{pll0}}) = P\{\sin\theta_{\mathrm{pll0}}\}$, within which the nonzero components are $A_{\pm1} = \mp 0.5\mathrm{j} \cdot e^{\pm \mathrm{j}\delta_{\mathrm{pll0}}}$; whereas the nonzero components of $\boldsymbol{A}_{\cos}(\delta_{\mathrm{pll0}})$ are $A_{\pm1} = \pm 0.5 e^{\pm \mathrm{j}\delta_{\mathrm{pll0}}}$; $\boldsymbol{U}_{\mathrm{d0}} = P\{U_{\mathrm{d0}}\}$ is a diagonal matrix.

Since $\Delta\theta_{\mathrm{pll}}(s) = \dfrac{H_{\mathrm{pll}}(s)}{s} \Delta U_{\mathrm{q}}(s)$, substituting its HTF model into (A.3) yields

$$\Delta\boldsymbol{\theta}_{\mathrm{pll}}(s) = \boldsymbol{T}_{\mathrm{pll}}(s) \begin{bmatrix} -\boldsymbol{A}_{\sin}(\delta_{\mathrm{pll0}}) & \boldsymbol{A}_{\cos}(\delta_{\mathrm{pll0}}) \end{bmatrix} \begin{bmatrix} \Delta\hat{\boldsymbol{U}}_{\mathrm{a}}(s) \\ \Delta\hat{\boldsymbol{U}}_{b}(s) \end{bmatrix} \tag{A.4}$$

where $\boldsymbol{T}_{\text{pll}}(s)$ contains the frequency-shifted copies of $T_{\text{pll}(0)}=H_{\text{pll}}(s)/\left(s+U_{\text{d0}}H_{\text{pll}}(s)\right)$. Finally, combining (A.2) and (A.5) yields the HTF of the QSG-PLL

$$\Delta\boldsymbol{\theta}_{\text{pll}}(s)= \underbrace{\boldsymbol{T}_{\text{pll}}(s)\left[-\boldsymbol{A}_{\sin}\left(\delta_{\text{pll0}}\right)\quad \boldsymbol{A}_{\cos}\left(\delta_{\text{pll0}}\right)\right]\begin{bmatrix}\boldsymbol{H}_{\text{sogia}}(s)\\ \boldsymbol{H}_{\text{sogib}}(s)\end{bmatrix}}_{\boldsymbol{G}_{\theta\_u}(s)}\Delta\boldsymbol{U}_a(s) \quad \text{(A.5)}$$

2) Modeling of the dc voltage control

By linearizing the squared dc voltage, the HTF model of the dc voltage controller is obtained

$$\Delta\boldsymbol{I}_{\text{d}}^{\text{ref}}(s)=2\boldsymbol{H}_{\text{dc}}(s)\boldsymbol{U}_{\text{dc0}}\cdot\Delta\boldsymbol{U}_{\text{dc}}(s) \quad \text{(A.6)}$$

where $\boldsymbol{U}_{\text{dc0}}=P\left\{U_{\text{dc0}}(t)\right\}$. $U_{\text{dc0}}(t)$ is the steady-state dc voltage usually containing even harmonics. $\boldsymbol{H}_{\text{dc}}(s)$ contains the frequency-shifted copies of H_{dc}.

Subsequently, the linearized ac current reference is

$$\Delta i_{\text{a}}^{\text{ref}}=\cos\theta_{\text{pll0}}\Delta i_{\text{d}}^{\text{ref}}-\sin\theta_{\text{pll0}}\Delta i_{\text{q}}^{\text{ref}}-I_{\text{b0}}^{\text{ref}}(t)\Delta\theta_{\text{pll}} \quad \text{(A.7)}$$

where $I_{\text{b0}}^{\text{ref}}(t)=\sin\theta_{\text{pll0}}I_{\text{d0}}^{\text{ref}}(t)+\cos\theta_{\text{pll0}}I_{\text{q0}}^{\text{ref}}(t)$, $I_{\text{d0}}^{\text{ref}}(t)$ and $I_{\text{d0}}^{\text{ref}}(t)$ are steady-state d-axis and q-axis current references. Since this work assumes a constant reactive current control, thus $\Delta i_{\text{q}}^{\text{ref}}=0$, so that the HTF model of (A.7) is obtained as

$$\Delta\boldsymbol{I}_{\text{a}}^{\text{ref}}=\boldsymbol{A}_{\cos}\left(\delta_{\text{pll0}}\right)\Delta\boldsymbol{I}_{\text{d}}^{\text{ref}}-\boldsymbol{I}_{\text{b0}}^{\text{ref}}\Delta\boldsymbol{\theta}_{\text{pll}} \quad \text{(A.8)}$$

where $\boldsymbol{I}_{\text{b0}}^{\text{ref}}=P\left\{\sin\theta_{\text{pll0}}I_{\text{d0}}^{\text{ref}}(t)+\cos\theta_{\text{pll0}}I_{\text{q0}}^{\text{ref}}(t)\right\}$.

Then, combining (A.4), (A.6) and (A.8), the following relation is obtained:

$$\Delta\boldsymbol{I}_{\text{a}}^{\text{ref}}(s)= 2\boldsymbol{A}_{\cos}\left(\delta_{\text{pll0}}\right)\boldsymbol{H}_{\text{dc}}(s)\boldsymbol{U}_{\text{dc0}}\cdot\Delta\boldsymbol{U}_{\text{dc}}(s)-\boldsymbol{I}_{\text{b0}}^{\text{ref}}\boldsymbol{G}_{\theta\_u}(s)\Delta\boldsymbol{U}_{\text{a}}(s) \quad \text{(A.9)}$$

3) Modeling of the current control

The HTF model of the ac current control is

$$\Delta\boldsymbol{U}_{\text{a}}^{\text{ref}}(s)=\boldsymbol{H}_{\text{PR}}(s)\cdot\left(\Delta\boldsymbol{I}_{\text{a}}^{\text{ref}}(s)-\Delta\boldsymbol{I}_{\text{a}}(s)\right) \quad \text{(A.10)}$$

Then, considering a second-order *Pade* approximation of the control and PWM delay

$$G_{\text{del}}(s)=\frac{1-\frac{3T_{\text{d}}}{4}s+\frac{T_{\text{d}}^2}{4}s^2}{1+\frac{3T_{\text{d}}}{4}s+\frac{T_{\text{d}}^2}{4}s^2} \quad \text{(A.11)}$$

the HTFs of the CM and DM cases are obtained as

$$\begin{cases}\Delta\boldsymbol{M}_{\text{a}}^{\text{DM}}=\dfrac{1}{V_{\text{dc}}^{\text{ref}}}\boldsymbol{G}_{\text{del}}(s)\Delta\boldsymbol{U}_{\text{a}}^{\text{ref}}(s)\\ \Delta\boldsymbol{M}_{\text{a}}^{\text{CM}}=\boldsymbol{G}_{\text{del}}(s)\boldsymbol{U}_{\text{dc0}}^{-1}\left(\Delta\boldsymbol{U}_{\text{a}}^{\text{ref}}(s)-\boldsymbol{M}_{0}^{\text{ref}}\Delta\boldsymbol{U}_{\text{dc}}(s)\right)\end{cases} \quad \text{(A.12)}$$

where $m_{a0}^{ref}(t)$ is the steady-state modulation index, and $\boldsymbol{M}_0^{ref}=P\{m_{a0}^{ref}(t)\}$ is its Toeplitz matrix. $\boldsymbol{G}_{\text{del}}(s)$ contains the frequency-shifted copies of $G_{\text{del}}(s)$.

4) Modeling of the VSC circuit

According to Fig. 1 (a), the linearized state-space model of the main circuit is

$$\frac{d}{dt}\Delta X_{\text{c}}=A_{\text{c}}(t)\Delta X_{\text{c}}+B_m(t)\Delta m_{\text{a}}^{\text{ref}}+B_u u_{\text{a}} \quad \text{(A.13)}$$

where $\Delta X_{\text{c}}=\begin{bmatrix}\Delta u_{\text{dc}}\\ \Delta i_{\text{a}}\end{bmatrix}$, $A_{\text{c}}(t)=\begin{bmatrix}-\dfrac{1}{R_L C_{\text{cap}}} & -\dfrac{m_{\text{a0}}^{\text{ref}}(t)}{C_{\text{cap}}}\\ \dfrac{m_{\text{a0}}^{\text{ref}}(t)}{L_{\text{f}}} & -\dfrac{R_{\text{f}}}{L_{\text{f}}}\end{bmatrix}$,

$B_m(t)=\left[-\dfrac{i_{\text{a0}}(t)}{C_{\text{cap}}},\dfrac{u_{\text{dc0}}(t)}{L_{\text{f}}}\right]^T$, and $B_u=\left[0,-\dfrac{1}{L_{\text{f}}}\right]^T$.

Transforming (A.14) into harmonic domain yields

$$\begin{aligned}&\left(s\boldsymbol{I}+\boldsymbol{N}_{\text{blk}}\right)\Delta\boldsymbol{X}_{\text{c}}(s)\\ &=\boldsymbol{A}_{\text{c}}\Delta\boldsymbol{X}_{\text{c}}(s)+\boldsymbol{B}_{\text{m}}\Delta\boldsymbol{M}_{\text{a}}^{\text{ref}}(s)+\boldsymbol{B}_{\text{u}}\Delta\boldsymbol{U}_{\text{a}}(s)\end{aligned} \quad \text{(A.14)}$$

where $\boldsymbol{N}_{\text{blk}}=diag\left(\cdots,-\text{kj}\omega_1\boldsymbol{I}_{2\times2},\cdots,\boldsymbol{0}_{2\times2},\cdots,\text{kj}\omega_1\boldsymbol{I}_{2\times2},\cdots\right)$ is a block diagonal matrix; $\boldsymbol{A}_{\text{c}}$, $\boldsymbol{B}_{\text{m}}$, and $\boldsymbol{B}_{\text{u}}$ are the Toeplitz matrices of $A_{\text{c}}(t)$, $B_{\text{m}}(t)$ and B_u; $\Delta\boldsymbol{X}_{\text{c}}(s)=\left[\ldots,\Delta X_{\text{c}(-1)},\Delta X_{\text{c}(0)},\Delta X_{\text{c}(+1)},\ldots\right]^T$; $\Delta\boldsymbol{M}_{\text{a}}^{\text{ref}}(s)$ and $\Delta\boldsymbol{U}_{\text{a}}(s)$ are in a similar format as $\Delta\boldsymbol{X}_{\text{c}}(s)$.

Finally, by assembling HTFs (A.8)-(A.12) and (A.14), the VSC harmonic-domain admittance $\boldsymbol{Y}_{\text{c}}^{\text{HTF}}(s)$ is established.

B. Proof of the identical stability conclusion of the SISO equivalent and MIMO original system

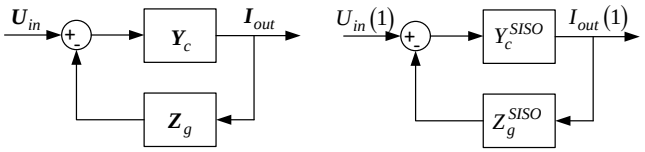

(a) MIMO-model based closed-loop system

(b) Equivalent SISO-model based closed-loop system

Fig. A1 The MIMO and SISO equivalent model-based source and load system

To achieve a clear comparison in forthcoming analysis, the detailed models of the grid and VSC are assumed to be 2-by-2 matrices. This will not compromise the generality if higher-dimensional matrices are analyzed.

Suppose the grid and VSC model are developed as $\boldsymbol{Z}_g=\begin{bmatrix}Z_{g11} & Z_{g12}\\ Z_{g21} & Z_{g22}\end{bmatrix}$, $\boldsymbol{Y}_c=\begin{bmatrix}Y_{c11} & Y_{c12}\\ Y_{c21} & Y_{c22}\end{bmatrix}$. According to Fig.A1 (a), the closed-loop model for the MIMO system is

$$\boldsymbol{I}_{out}=\left(\boldsymbol{I}+\boldsymbol{Y}_c\boldsymbol{Z}_g\right)^{-1}\boldsymbol{Y}_c\boldsymbol{U}_{ptb}=\left(\boldsymbol{Z}_c+\boldsymbol{Z}_g\right)^{-1}\boldsymbol{U}_{ptb} \quad \text{(A.15)}$$

Then, the characteristic equation C_{MIMO} of this MIMO system is obtained from the numerator of $\det\left(\boldsymbol{Z}_c+\boldsymbol{Z}_g\right)$, which is

$$C_{MIMO}=\mathcal{N}\begin{Bmatrix}\left(Z_{g11}+Z_{c11}\right)\left(Z_{g22}+Z_{c22}\right)\\ -\left(Z_{g12}+Z_{c12}\right)\left(Z_{g21}+Z_{c21}\right)\end{Bmatrix} \quad \text{(A.16)}$$

where $\mathcal{N}\{\cdot\}$ is defined as an operator extracting the numerator of a *s*-domain function.

Further, based on the SISO modeling technique, the VSC and grid- SISO equivalent model evaluated under the first input of U_{in} and the first output I_{out} are derived as:

$$\begin{cases} Z_g^{SISO} = Z_{g11} - Z_{g12}\dfrac{Z_{c21}+Z_{g21}}{Z_{c22}+Z_{g22}} \\ Z_c^{SISO} = Z_{c11} - \dfrac{Z_{c12}\left(Z_{c21}+Z_{g21}\right)}{Z_{c22}+Z_{g22}} \end{cases} \tag{A.17}$$

Corresponding closed-loop model based on Fig.A1 (b) is

$$I_{out}(1) = \left(1+Y_c^{SISO}Z_g^{SISO}\right)^{-1} Y_c^{SISO}U_{ptb}(1) = \left(Z_c^{SISO}+Z_g^{SISO}\right)^{-1}U_{ptb}(1) \tag{A.18}$$

Then, the characteristic equation C_{SISO} of this SISO equivalent system is obtained as $\mathcal{N}\left\{Z_c^{SISO}+Z_g^{SISO}\right\}$, which is

$$C_{SISO} = \mathcal{N}\left\{\frac{\left(Z_{g11}+Z_{c11}\right)\left(Z_{c22}+Z_{g22}\right)-\left(Z_{c21}+Z_{g21}\right)\left(Z_{g12}+Z_{c12}\right)}{Z_{c22}+Z_{g22}}\right\} \tag{A.19}$$

It should be noted that all the components, e.g. Z_{g11}, Z_{c11} are functions as $Z_{g11} = \dfrac{N_{g11}(s)}{D_{g11}(s)}$. Since the denominator of $Z_{c22}+Z_{g22}$ also appears in the denominator of $\left(Z_{g11}+Z_{c11}\right)\left(Z_{c22}+Z_{g22}\right)-\left(Z_{c21}+Z_{g21}\right)\left(Z_{g12}+Z_{c12}\right)$, thus they are canceled in (A.19). Based on this, it obtains

$$C_{SISO} = \mathcal{N}\left\{\begin{matrix}\left(Z_{g11}+Z_{c11}\right)\left(Z_{c22}+Z_{g22}\right) \\ -\left(Z_{c21}+Z_{g21}\right)\left(Z_{g12}+Z_{c12}\right)\end{matrix}\right\} \tag{A.20}$$

By comparing (A.16) and (A.20)

$$C_{SISO} = C_{MIMO} \tag{A.21}$$

is obtained and the proof is done. This derivation also shows that the SISO impedance modeling technique is applicable to a grid exhibiting frequency coupling behavior.

REFERENCES

[1] Teodorescu R, Liserre M, Rodriguez P. "Introduction," in Grid converters for photovoltaic and wind power systems. Chichester, United Kingdom: John Wiley & Sons, 2011, pp:1-4.

[2] Flourentzou N, Agelidis V G, Demetriades G D. "VSC-Based HVDC Power Transmission Systems: An Overview," IEEE Trans. Power Electron, vol.24, no.3, pp.592-602, 2009.

[3] H. Hu, Y. Shao, L. Tang, J. Ma, Z. He and S. Gao, "Overview of Harmonic and Resonance in Railway Electrification Systems," in IEEE Transactions on Industry Applications, vol. 54, no. 5, pp. 5227-5245, Sept.-Oct. 2018.

[4] H. Liu, X. Xie, J. He, T. Xu, Z. Yu, C. Wang, C.Zhang. Subsynchronous interaction between direct-drive PMSG based wind farms and weak AC networks. IEEE Transactions on Power Systems, 32(6), 4708-4720, 2017.

[5] C. Li, "Unstable Operation of Photovoltaic Inverter From Field Experiences," in IEEE Transactions on Power Delivery, vol. 33, no. 2, pp. 1013-1015, April 2018.

[6] Sun. J. "Impedance-Based Stability Criterion for Grid-Connected Inverters," in IEEE Transactions on Power Electronics, vol. 26, no. 11, pp. 3075-3078, Nov. 2011.

[7] X. Wang and F. Blaabjerg, "Harmonic Stability in Power Electronic-Based Power Systems: Concept, Modeling, and Analysis," in IEEE Transactions on Smart Grid, vol. 10, no. 3, pp. 2858-2870, May 2019.

[8] L. Harnefors, "Modeling of Three-Phase Dynamic Systems Using Complex Transfer Functions and Transfer Matrices," in IEEE Transactions on Industrial Electronics, vol. 54, no. 4, pp. 2239-2248, Aug. 2007.

[9] Belkhayat M, "Stability criteria for AC power systems with regulated loads," Ph.D. dissertation, Purdue University, USA, 1997.

[10] B. Wen, D. Boroyevich, R. Burgos, P. Mattavelli and Z. Shen, "Small-Signal Stability Analysis of Three-Phase AC Systems in the Presence of Constant Power Loads Based on Measured d-q Frame Impedances," in IEEE Transactions on Power Electronics, vol. 30, no. 10, pp. 5952-5963, Oct. 2015.

[11] L. Harnefors, M. Bongiorno and S. Lundberg, "Input-Admittance Calculation and Shaping for Controlled Voltage-Source Converters," in IEEE Transactions on Industrial Electronics, vol. 54, no. 6, pp. 3323-3334, Dec. 2007.

[12] A. Gelb, W. E. V. Velde, Multiple-Input Describing Functions and Nonlinear System Design, New York:McGraw-Hill, 1968.

[13] A. Lesnicar, and R. Marquardt: An Innovative Modular Multilevel Converter Topology Suitable for a Wide Power Range, IEEE PowerTech Conference, Bologna, Italy, June 23-26, 2003.

[14] H. Zhang, Z. Liu, S. Wu and Z. Li, "Input Impedance Modeling and Verification of Single-Phase Voltage Source Converters Based on Harmonic Linearization," in IEEE Transactions on Power Electronics, vol. 34, no. 9, pp. 8544-8554, Sept. 2019.

[15] M. Cespedes and J. Sun, "Impedance Modeling and Analysis of Grid-Connected Voltage-Source Converters," in IEEE Transactions on Power Electronics, vol. 29, no. 3, pp. 1254-1261, March 2014.

[16] J. Sun and H. Liu, "Sequence Impedance Modeling of Modular Multilevel Converters," in *IEEE Journal of Emerging and Selected Topics in Power Electronics*, vol. 5, no. 4, pp. 1427-1443, Dec. 2017.

[17] X. Wang, L. Harnefors, F. Blaabjerg, and P.C. Loh, "A Unified Impedance Model of Voltage-Source Converters with Phase-Locked Loop Effect," IEEE ECCE, United States, pp. 1–8, 2016.

[18] A. Rygg, M. Molinas, C. Zhang and X. Cai, "A Modified Sequence-Domain Impedance Definition and Its Equivalence to the dq-Domain Impedance Definition for the Stability Analysis of AC Power Electronic Systems," in IEEE Journal of Emerging and Selected Topics in Power Electronics, vol. 4, no. 4, pp. 1383-1396, Dec. 2016

[19] M. Kazem Bakhshizadeh et al., "Couplings in Phase Domain Impedance Modeling of Grid-Connected Converters," in IEEE Transactions on Power Electronics, vol. 31, no. 10, pp. 6792-6796, Oct. 2016.

[20] Wereley, N. M.. Analysis and control of linear periodically time varying systems, Diss. Massachusetts Institute of Technology, 1990.

[21] Vanassche, P., Gielen, G., & Sansen, W. M. Systematic modeling and analysis of telecom frontends and their building blocks. Springer Science & Business Media, 2006.

[22] J. Kwon, X. Wang, F. Blaabjerg, C. L. Bak, V. Sularea and C. Busca, "Harmonic Interaction Analysis in a Grid-Connected Converter Using Harmonic State-Space (HSS) Modeling," in IEEE Transactions on Power Electronics, vol. 32, no. 9, pp. 6823-6835, Sept. 2017.

[23] J. Kwon, X. Wang, C. L. Bak and F. Blaabjerg, "Harmonic instability analysis of single-phase grid connected converter using Harmonic State Space (HSS) modeling method," 2015 IEEE Energy Conversion Congress and Exposition (ECCE), Montreal, QC, 2015, pp. 2421-2428.

[24] J. Lyu, X. Zhang, X. Cai and M. Molinas, "Harmonic State-Space Based Small-Signal Impedance Modeling of a Modular Multilevel Converter With Consideration of Internal Harmonic Dynamics," in IEEE Transactions on Power Electronics, vol. 34, no. 3, pp. 2134-2148, March 2019.

[25] H. Wu, X. Wang and Ł. Kocewiak, "Impedance-Based Stability Analysis of Voltage-Controlled MMCs Feeding Linear AC Systems," in IEEE Journal of Emerging and Selected Topics in Power Electronics, 2019 (early access), doi: 10.1109/JESTPE.2019.2911654.

[26] H. Wang, M. Wu and J. Sun, "Analysis of Low-Frequency Oscillation in Electric Railways Based on Small-Signal Modeling of Vehicle-Grid

System in dq Frame," in IEEE Transactions on Power Electronics, vol. 30, no. 9, pp. 5318-5330, Sept. 2015.
[27] Y. Liao, Z. Liu, H. Zhang and B. Wen, "Low-Frequency Stability Analysis of Single-Phase System Withdq-Frame Impedance Approach—Part I: Impedance Modeling and Verification," in IEEE Transactions on Industry Applications, vol. 54, no. 5, pp. 4999-5011, Sept.-Oct. 2018.
[28] S. Lissandron, L. Dalla Santa, P. Mattavelli and B. Wen, "Experimental Validation for Impedance-Based Small-Signal Stability Analysis of Single-Phase Interconnected Power Systems With Grid-Feeding Inverters," in IEEE Journal of Emerging and Selected Topics in Power Electronics, vol. 4, no. 1, pp. 103-115, March 2016.
[29] S. Shah and L. Parsa, "On impedance modeling of single-phase voltage source converters," 2016 IEEE Energy Conversion Congress and Exposition (ECCE), Milwaukee, WI, 2016, pp. 1-8.
[30] Q. Qian, S. Xie, J. Xu, K. Xu, S. Bian and N. Zhong, "Output Impedance Modeling of Single-Phase Grid-Tied Inverters with Capturing the Frequency-Coupling Effect of PLL," in IEEE Transactions on Power Electronics. doi: 10.1109/TPEL.2019.2946984
[31] J A. Antonopoulos, L. Angquist and H. Nee, "On dynamics and voltage control of the Modular Multilevel Converter," 2009 13th European Conference on Power Electronics and Applications, Barcelona, 2009, pp. 1-10.
[32] V. Salis, A. Costabeber, S. M. Cox and P. Zanchetta, "Stability Assessment of Power-Converter-Based AC systems by LTP Theory: Eigenvalue Analysis and Harmonic Impedance Estimation," in IEEE Journal of Emerging and Selected Topics in Power Electronics, vol. 5, no. 4, pp. 1513-1525, Dec. 2017.
[33] C. Zhang, X. Cai, A. Rygg and M. Molinas, "Sequence Domain SISO Equivalent Models of a Grid-Tied Voltage Source Converter System for Small-Signal Stability Analysis," in IEEE Transactions on Energy Conversion, vol. 33, no. 2, pp. 741-749, June 2018.

Chen Zhang received the B.Eng. degree from the China University of Mining and Technology, China, and the Ph.D. from Shanghai Jiao Tong University, China, in 2011 and 2018 respectively. He was a Ph.D. Visiting Scholar with the Department of Engineering Cybernetics, Norwegian University of Science and Technology, Norway, in 2015. Currently, he is a Postdoctoral Research Fellow at NTNU. His research interest is modeling and stability analysis of VSC-based energy conversion systems, where the aim is to reveal the fundamental dynamics and stability mechanisms of renewable energies with VSCs as the grid interface.

Marta Molinas (M'94) received the Diploma degree in electromechanical engineering from the National University of Asuncion, Asuncion, Paraguay, in 1992; the Master of Engineering degree from Ryukyu University, Japan, in 1997; and the Doctor of Engineering degree from the Tokyo Institute of Technology, Tokyo, Japan, in 2000. She was a Guest Researcher with the University of Padova, Padova, Italy, during 1998. From 2004 to 2007, she was a Postdoctoral Researcher with the Norwegian University of Science and Technology (NTNU) and from 2008-2014 she has been professor at the Department of Electric Power Engineering at the same university. She is currently Professor at the Department of Engineering Cybernetics, NTNU. Her research interests include stability of power electronics systems, harmonics, instantaneous frequency, and non-stationary signals from the human and the machine. She is Associate Editor for the IEEE Journal JESTPE, IEEE PELS Transactions and Editor of the IEEE Transactions on Energy Conversion. Dr. Molinas has been an AdCom Member of the IEEE Power Electronics Society from 2009 to 2011.

Sjur Føyen (M'18) received the Master degree in electric power engineering from the Norwegian University of Science and Technology, Trondheim, Norway, in 2018. Currently, he is pursuing his doctoral degree in power electronics synchronisation and stability. His research interests include synchronisation, time-frequency analysis and stability of power (electronics) systems.

Jon Are Suul (M'11) received the M.Sc. degree in energy and environmental engineering and the Ph.D. degree in electric power engineering from the Norwegian University of Science and Technology (NTNU), Trondheim, Norway, in 2006 and 2012, respectively. From 2006 he was with SINTEF Energy Research, Trondheim, where he was working with simulation of power electronic converters and marine propulsion systems until starting his PhD studies. From 2012, he resumed a position as a Research Scientist at SINTEF Energy Research, first in part-time position while also working as a part-time postdoctoral researcher at the Department of Electric Power Engineering of NTNU until 2016. Since August 2017, he is serving as an Adjunct Associate Professor at the Department of Engineering Cybernetic of NTNU. His research interests are mainly related to modelling, analysis and control of power electronic converters in HVDC transmission systems, renewable energy applications and electrification of transport. Dr. Suul is an Associate Editor for the IEEE JOURNAL OF EMERGING AND SELECTED TOPICS IN POWER ELECTRONICS.

Takanori Isobe (M'07) was born in Hamamatsu, Japan, in 1978. He received the B.Eng. degree in physical electronics, the M.Eng. degree in nuclear engineering, and the D.Eng. degree in energy sciences from the Tokyo Institute of Technology, Tokyo, Japan, in 2003, 2005, and 2008, respectively. From 2008 to 2010 and from 2012 to 2013, he was a Researcher with the Tokyo Institute of Technology, where from 2010 to 2012, he was an Assistant Professor. From 2013 to 2014, he was with MERSTech, Tokyo. In 2013, he joined the University of Tsukuba, Tsukuba, Ibaraki, Japan, where he is currently an Associate Professor at the Faculty of Pure and Applied Sciences. His research interests include static reactive power compensators and soft-switching power converters. Dr. Isobe is a Member of the Institute of Electrical Engineers of Japan and the Japan Institute of Power Electronics.